energy&fuels

pubs.acs.org/EF

Article

Dual-Functional Al-Doped Co_xS_v Nanoneedle Arrays: Enhanced Supercapacitive Energy Storage and Electrocatalytic Water Splitting

Heran Ren, Kai Jia,* Zihan Lv, Zhiqiang Yin, Songlin Xu, Huiya Zhou, Rong-Da Zhao,* Depeng Zhao,* and Lihua Miao*

Cite This: *Energy Fuels* 2026, 40, 3770−3780

Read Online

ACCESS | Metrics & More | Article Recommendations

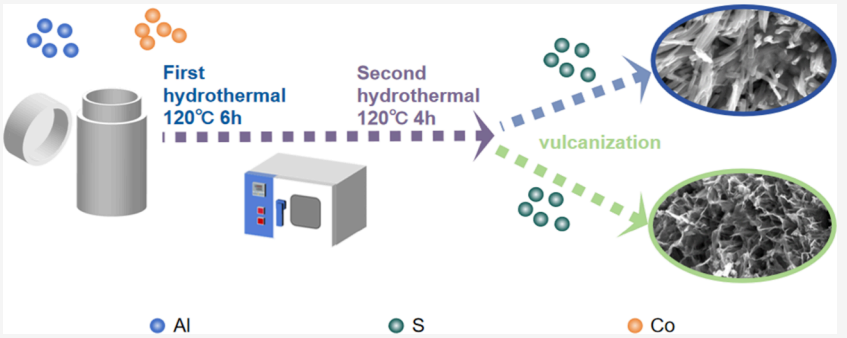

ABSTRACT: Against the backdrop of escalating global energy demands and the gradual depletion of conventional fossil fuels, water electrolysis has emerged as a pivotal pathway for achieving clean and sustainable hydrogen utilization. In this study, Co_xS_v nanomaterials were successfully synthesized via a facile hydrothermal method. Strategic incorporation of aluminum ions induced structural modifications, effectively augmenting both specific surface area and active site density, thereby substantially enhancing the electrochemical performance of the electrode materials. Experimental results demonstrate that the Al-doped Co_xS_v electrode with 0.45 mmol Al addition achieves an exceptional areal capacitance of 418.2 $C \cdot cm^{-2}$, showcasing superior supercapacitive behavior. Notably, the optimized Al−Co_xS_v electrode with 0.15 mmol Al doping exhibits a significantly reduced hydrogen evolution overpotential of 228.3 mV at 10 $mA \cdot cm^{-2}$, highlighting remarkable electrocatalytic enhancement.

1. INTRODUCTION

Supercapacitors, with their high power density, long-cycle stability, and high safety, are widely recognized as one of the most promising energy storage devices. However, their energy density is far lower than that of batteries. Based on this, pseudocapacitors have been extensively and intensively studied due to their high specific capacitance and excellent energy density characteristics. Therefore, exploring pseudocapacitive materials with high specific capacitance as electrodes is of vital significance for meeting the performance requirements of energy storage devices.[1−6]

At present, environmental problems are becoming increasingly severe, and the energy problem is also extremely urgent. Given the huge potential of hydrogen energy, it is regarded as an ideal alternative to other traditional energy sources. However, the practical application of hydrogen is hampered by challenges in storage, transportation, and production, as well as its dependence on limited natural gas resources.[7−12] Noble metal materials, as a type of high-quality electrocatalytic materials, often exhibit outstanding electrocatalytic performance, which is specifically manifested in low overpotential, low Tafel slope, and excellent stability. For example, RuIr, RuO_2, and IrO_2 are recognized as the most excellent catalysts for the Oxygen-Evolution Reaction (OER) due to their excellent properties. Similarly, noble metal Pt and its oxides also perform remarkably in the Hydrogen Evolution Reaction (HER) catalysis.[12] Although noble metal catalysts demonstrate significant advantages such as low overpotential and high stability in the field of electrocatalysis, their high cost and limited reserves have become serious obstacles to large-scale applications. In view of this, researchers are committed to exploring non-noble metal catalysts with excellent performance and low cost.

Transition metal oxides, such as perovskite, rutile, and spinel oxides, have attracted extensive attention in the field of electrocatalysis due to their abundant reserves in the earth's

Received: September 20, 2025
Revised: January 28, 2026
Accepted: January 30, 2026
Published: February 11, 2026

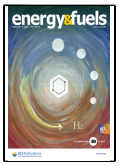

https://doi.org/10.1021/acs.energyfuels.5c04896
Energy Fuels 2026, 40, 3770−3780

crust, excellent stability, strong corrosion resistance, and ease of preparation.[13−15] Transition metal sulfides are a type of semiconductor material similar to oxides. They have a relatively small valence-conduction band gap and usually possess excellent electrical conductivity, thus exhibiting unique physical and chemical properties.Pseudocapacitor electrode materials represented by transition metal oxides, sulfides, hydroxides, and conductive polymers have broad application prospects. Representative examples include Co_3O_4,[16] $NiCo_2O_4$,[17] $Ni(OH)_2$,[18] Ni_3S_2,[19] TiO_2,[39] Fe_2O_3[40] etc., as well as conductive polymers such as polyaniline (PANI), polythiophene, and polypyrrole.[20]

In heterogeneous catalytic systems, the redox reactions of metal species are the key factors affecting catalytic performance. Based on this, this project plans to conduct in-depth research from multiple dimensions such as crystal structure, chemical composition, defect degree, and element valence states.[21−23] Zhang et al.[33] successfully synthesized polyhedral cobalt disulfide (CoS_2) with cubic crystal structure through an innovative potassium halide-assisted solid-state assembly (SSA) method in a sealed silica tube system (850 °C, 9 h). By systematically introducing KX (X = Cl, Br, I) as flux agents and precisely controlling the reaction kinetics, well-defined polyhedral crystals with uniform size distribution were obtained.

Phase evolution studies revealed that the crystal structure undergoes significant transformations under different thermal treatment conditions: the material maintains stable cubic CoS_2 phase at 400 °C, begins to transform into tetragonal Co_3S_4 at 500 °C, and completely converts to hexagonal CoS after 800 °C treatment. This phase transition process, accompanied by gradual sulfur extraction and crystal structure reconstruction, demonstrates the material's sensitive response to thermal conditions.

In recent years, transition metal-chalcogenide-based electrocatalysts, which are abundant on the earth, have played a crucial role in alkaline water splitting. In particular, cobalt chalcogenide (Co_xS_v), due to its metallic properties, variable valence states, and adjustable electronic configuration (d-orbitals), has become a potential bifunctional substitute for HER and OER.[41−44] However, under harsh electrolysis conditions, Co_xS_v has low intrinsic activity and poor long-term durability, and its overall water splitting performance still lags far behind that of noble metal electrocatalysts.[34−38] Al doping has many regulatory advantages in supercapacitors and electrocatalytic systems. In CoP systems, Al doping induces charge redistribution, generating electron-enriched active centers that enhance intrinsic HER activity.[31] For NiP catalysts, Al substitution at Ni sites not only optimizes crystalline structure but also increases porosity.[32]

The incorporation of heteroatoms can generate sufficient lattice vacancies, thereby increasing electrical conductivity and the number of active sites. In this context, doping Al into the Co_xS_v lattice is undoubtedly a task worthy of investment. It is expected to enhance the intrinsic activity through the synergistic modulation of the electronic state. And Carbon materials inherently possess superior electrical conductivity, enabling rapid electron transfer between catalysts and electrodes, thereby enhancing electrocatalytic efficiency. Moreover, their high specific surface area provides abundant active sites, while excellent corrosion resistance ensures structural stability under various conditions. Therefore, growing Al-doped Co_xS_v nanoarrays with abundant vacancies on carbon cloth is likely to create an opportunity to provide strong and stable performance for HER and OER. Moreover, the outstanding performance it exhibits in the field of supercapacitors is also of extremely great significance for future development.

2. EXPERIMENT

2.1. Synthesis of Co_xS_v Samples

This experiment aims to precisely control the doping amount of aluminum ions and conduct an in-depth exploration of its impact on the electrochemical performance of Co_xS_v electrode materials.

First, cut four pieces of carbon cloth with dimensions of 25 mm × 3.5 mm. Wash them repeatedly with deionized water and absolute ethanol multiple times to thoroughly remove surface impurities. After washing, dry the carbon cloth and reserve it for later use. Next, prepare the precursor solution. Dissolve 3.5 mmol of $Co(NO_3)_2{\cdot}6H_2O$, 18 mmol of $Co(NH_2)_2$, and 10 mmol of NH_4F in 60 mL of deionized water. Stir the solution well to ensure complete dissolution and form a homogeneous solution. Subsequently, take 0, 0.15, 0.30, and 0.45 mmol of $AlCl_3{\cdot}6H_2O$ respectively and dissolve them one by one in the abovementioned solution to obtain four experimental group solutions with different aluminum-ion doping concentrations. Stir each solution thoroughly to ensure uniform dispersion of the solutes, and label them as Al_0-Co_xS_v, $Al_{0.15}$-Co_xS_v, $Al_{0.3}$-Co_xS_v, and $Al_{0.45}$-Co_xS_v.Completely immerse the pretreated carbon cloth in the prepared solutions. Then, subject the reaction system to a hydrothermal reaction at 120 °C and maintain the temperature for 6 h. After the reaction is completed, take out the carbon cloth with $Co(OH)_2$ attached, wash it several times with deionized water to remove residual impurities on the surface, and then place it in a constant temperature oven at 60 °C for 6 h for drying.Weigh 0.35 g of sodium sulfide nonahydrate and dissolve it in 60 mL of deionized water. Stir the solution well to ensure complete dissolution. Put the dried experimental group samples together with the abovementioned sodium sulfide solution into a high-pressure reactor. After sealing the reactor, place it in an electrothermal blast drying oven and conduct a sulfurization reaction at 120 °C for 4 h. After the sulfurization reaction is finished, take out the samples, and perform washing and drying treatments again. Thus, Co_xS_v samples are successfully prepared.

2.2. Structure Characterization

The crystal structure and phase purity of the samples were determined using X-ray diffraction (XRD, 7000, Shimadzu). Sample morphology and structure were characterized using scanning electron microscopy (SEM, Gemini 300−71−31). X-ray photoelectron spectroscopy (XPS, ESCALAB 250 with an Al Kα), scanning electron microscopy (SEM, Gemini 300−71−31) and transmission electron microscopy (TEM, JEM-2100 PLUS).

2.3. Electrocatalytic Performance Characterization

All electrocatalytic performances were tested on a CHI660E electrochemical workstation. A standard three-electrode system was used in 1 M KOH (pH = 13.7) and 1 M KOH seawater solution (pH = 13.51) electrolytes. The prepared samples served as working electrodes, Ag/AgCl as the reference electrode, and Pt foil/carbon rod as counter electrodes for OER and HER, respectively. Cyclic voltammetry (CV), linear

https://doi.org/10.1021/acs.energyfuels.5c04896
Energy Fuels 2026, 40, 3770−3780

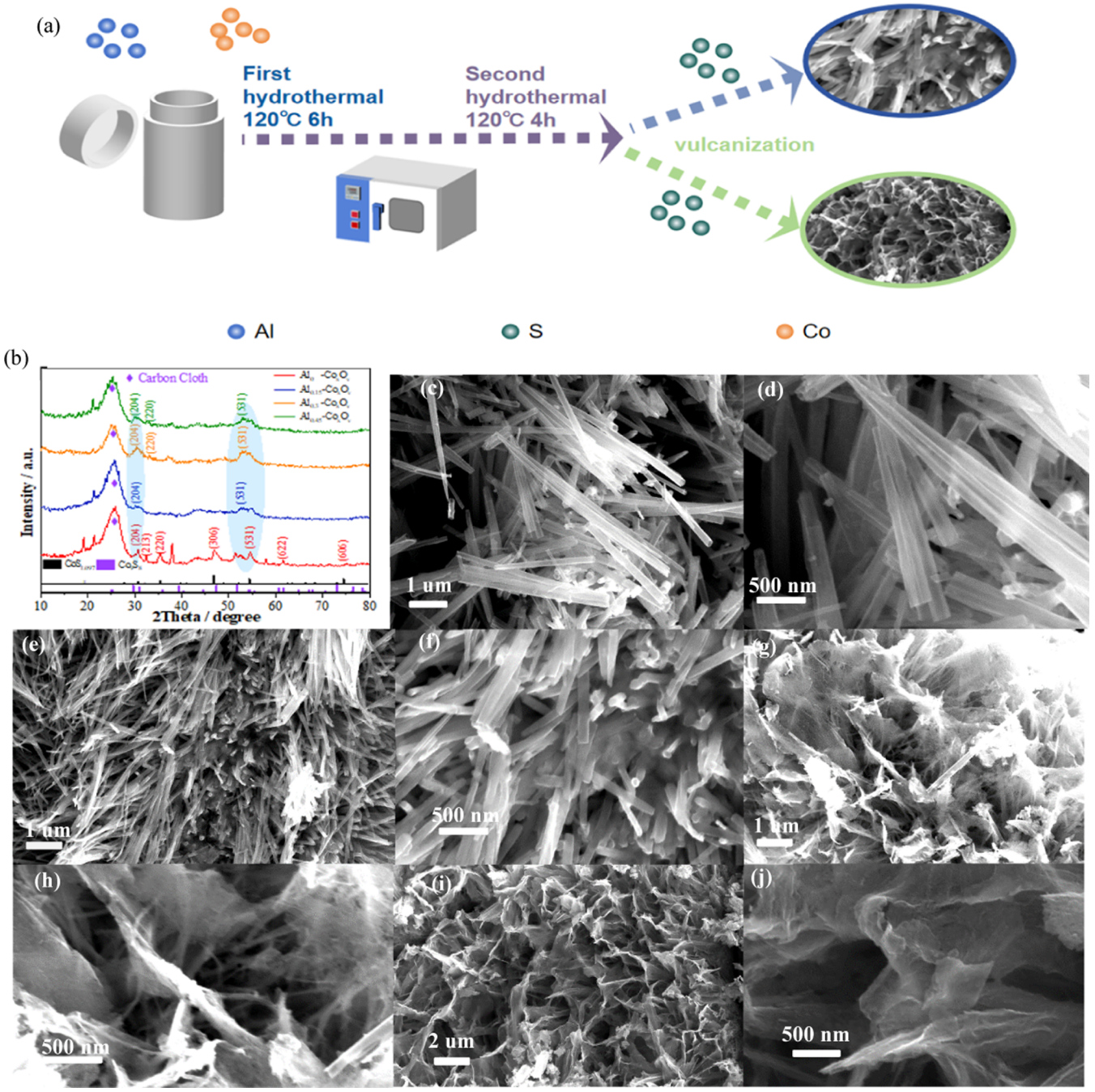

Figure 1. (a) Structure characterization of as-prepared electrocatalysts. (b) XRD pattern of the Al−Co_xS_v nanomaterial. (c, d) SEM images of the Co_xS_v nanomaterial. (e, f) SEM images of the 0.15 mmol Al−Co_xS_v nanomaterial. (g, h) SEM images of the 0.3 mmol Al−Co_xS_v nanomaterial. (i, j) SEM images of the 0.45 mmol Al−Co_xS_v nanomaterial.

sweep voltammetry (LSV), electrochemical impedance spectroscopy (EIS), and cycling stability tests (*i-t*) were conducted. The following formula was used to convert HER and OER voltages to RHE-related values: E(vs RHE) = E(vs Hg/HgO) + 0.059*pH + 0.098 V. Additionally, overall water splitting performance was tested using a two-electrode system with a scan rate of 5 mV s^{-1}.

3. RESULTS AND DISCUSSION

The crystal phase structure and composition of the samples in the experiment were determined by X-ray diffraction (XRD). Figure 1b shows the XRD characterization results of the prepared Co_xS_v materials doped with different amounts of Al ions. It can be seen that in this pattern, the red, blue, orange, and green lines represent the Co_xS_v materials doped with 0, 0.15, 0.3, and 0.45 mmol of Al ions, respectively. The peaks marked with diamonds are the characteristic peaks of the carbon cloth material. The five main peaks appearing at 30.9°, 32.0°, 35.5°, 47.0°, and 74.7° correspond to the (204), (213), (220), (306), and (606) crystal planes of the $CoS_{1.097}$ crystal (JCPDS no. 19−0366) respectively; while the two peaks at 25.2° and 54.5° correspond to the (220) and (531) crystal planes of the Co_9S_8 crystal (JCPDS no.02−1459) respectively.

https://doi.org/10.1021/acs.energyfuels.5c04896
Energy Fuels 2026, 40, 3770−3780

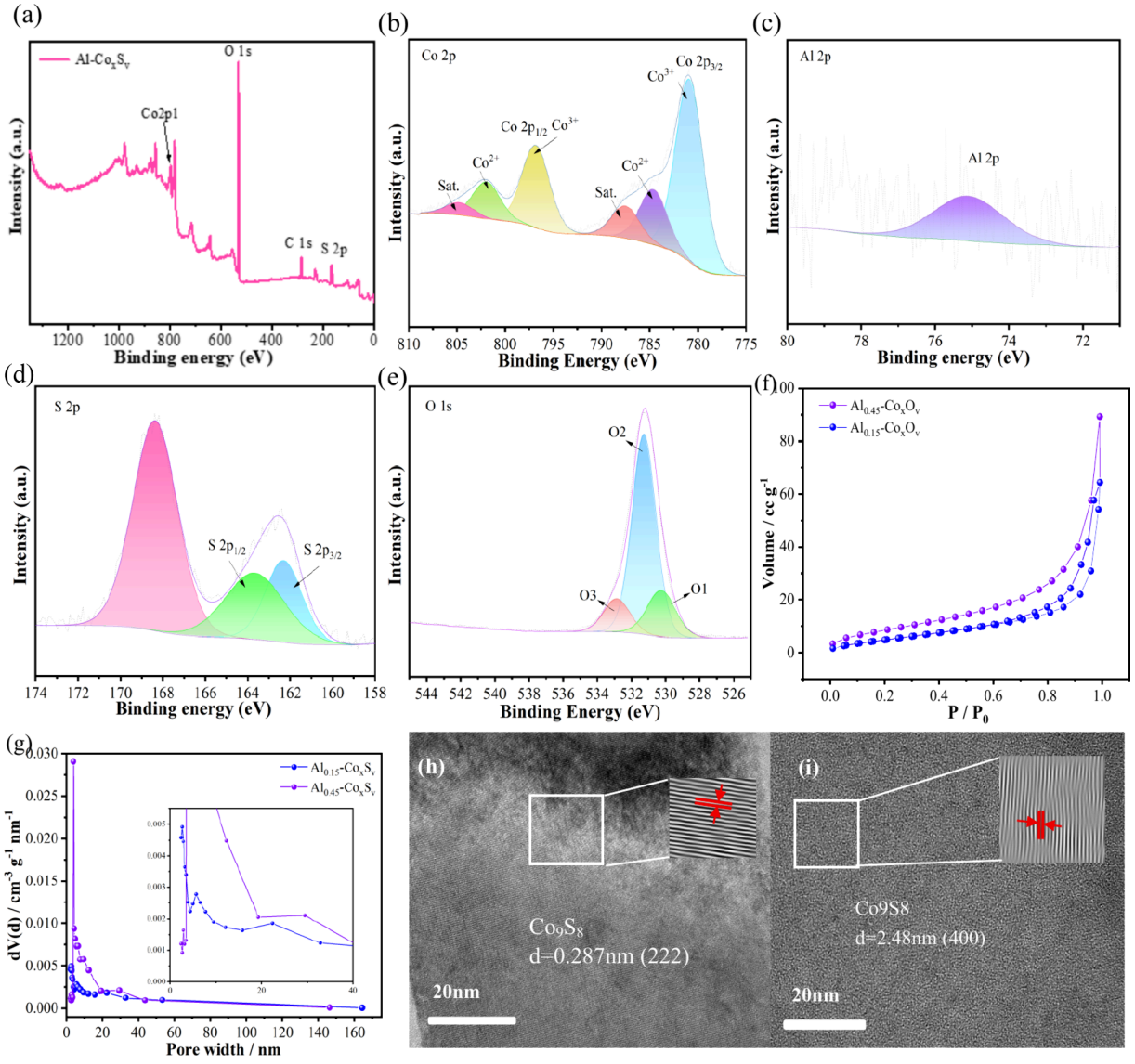

Figure 2. Structure characterization of as-prepared electrocatalysts. (a) Content of different elements. (b) XPS of Co 2p. (c) XPS of Al 2p. (d) XPS of S 2p. (e) XPS of O 1s. (f) N_2 adsorption−desorption isotherm of $Al_{0.15}$-Co_xO_v. (g) N_2 adsorption−desorption isotherm of $Al_{0.45}$-Co_xO_v. (h) Pore size distribution.

This result indicates that the main products of our experiment include $CoS_{1.097}$ and Co_9S_8 nanomaterials.

In addition, the (204) crystal plane of the $CoS_{1.097}$ crystal (JCPDS no.19−0366) originally at 30.9° and the (531) crystal plane of the Co_9S_8 crystal (JCPDS no.02−1459) originally at 54.5° show an obvious left-shift phenomenon after the doping treatment, with a decrease in θ. This indicates that the doping of Al ions expands the inter-planar spacing of the material.

The morphological characteristics of the prepared Co_xS_v nanomaterials were observed using scanning electron microscopy images. As shown in Figure 1c,d, the obtained Al−Co_xS_v nanomaterial samples have a regular nanoneedle structure, which is similar to the structure of Co_3O_4 before sulfidation.

From Figure 1e,f, we can clearly see that the Al−Co_xS_v nanomaterial doped with 0.15 mmol of Al ions still maintains a regular nanoneedle structure, but there are a small number of vacancies in the nanorod array. This is because the doping of Al ions causes a structural shift in the originally densely arranged Al−Co_xS_v nanorod structure, which provides a larger contact area for the electrochemical reaction. However, as the doping amount of Al ions increases, the originally densely arranged Al−Co_xS_v nanorod structure undergoes more structural changes. While this provides more reactive active sites for the electrochemical reaction, it greatly changes the original structure of the Al−Co_xS_v nanomaterial. As can be clearly seen from Figure 1g,j, with the increase in the doping amount of Al ions, the regular nanorod array of the Al−Co_xS_v nanomaterial transforms into a nanosheet structure.

The XPS survey spectrum (Figure 2a) identifies five constituent elements in Al−Co_xS_v: Co (797.08 eV), O (531.08 eV), C (285.08 eV), S (168.08 eV), and Al (68.08 eV). The high-resolution Co 2p spectrum (Figure 2b) exhibits multivalent cobalt characteristics: The characteristic peaks of Co^{2+} appear at 810.98 and 784.68 eV, while those of Co^{3+} are located at 796.38 and 781.08 eV. Figure 2c was fitted with a single peak, and the binding energy was 75.15 eV. Its binding energy is significantly higher than the characteristic peak of metallic Al (72.3 ∼ 73 eV), which may be due to the strong interaction with adjacent sulfur atoms to form an Al−O−S coordination structure. The peak deconvolution results of the

https://doi.org/10.1021/acs.energyfuels.5c04896
Energy Fuels 2026, 40, 3770−3780

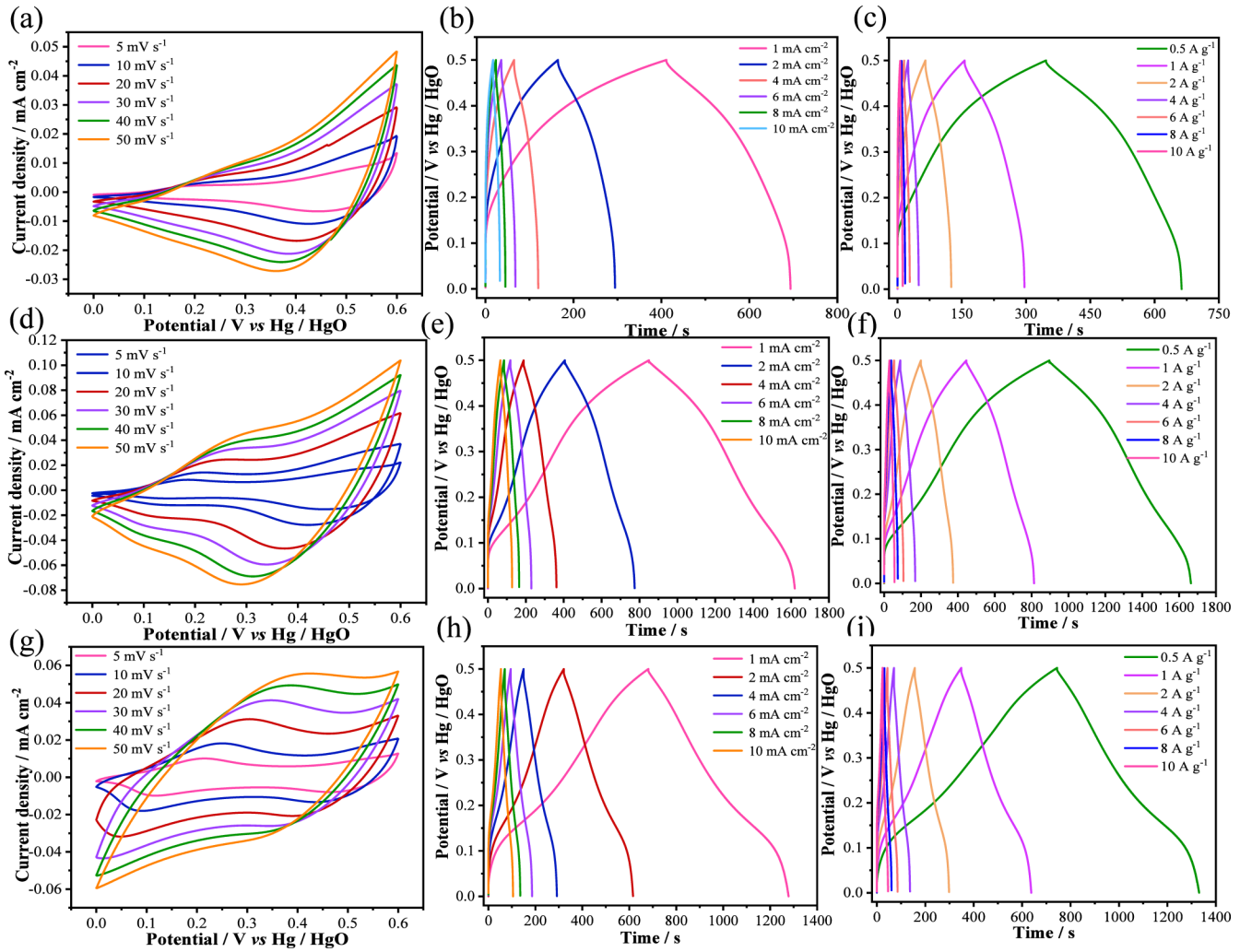

Figure 3. (a–c) CV and GCD curves of sample Al_0-Co_xS_v. (d–f) CV and GCD curves of sample $Al_{0.15}$-Co_xS_v. (g–i) CV and GCD curves of sample $Al_{0.3}$-Co_xS_v.

S 2p spectrum (Figure 2d) show typical chalcogen doublet characteristics: S $2p_{3/2}$ and S $2p_{1/2}$ are located at 162.68 and 163.68 eV respectively. The binding energy indicates the formation of metal–sulfur chemical bonds, confirming that the S element has been effectively incorporated into the Al–Co_xS_v lattice. After peak deconvolution, the O 1s spectrum (Figure 2e) exhibits three oxygen species: lattice oxygen (O1:530.28 eV), surface adsorbed oxygen (O2:531.28 eV), and oxygen at defect sites (O3:532.88 eV), revealing the rich active sites on the surface of the material. BET test were employed to evaluate the specific surface area and pore architecture of the materials. The isotherm of $Al_{0.15}$-Co_xO_v (Figure 2f) is of type IV with an H3 hysteresis loop, giving a multipoint BET surface area of 20.6 $m^2\ g^{-1}$. When the Al content was raised to $Al_{0.45}$-Co_xO_v, the surface area increased markedly to 34.3 m2 g-1. This gain is expected to expose a higher density of accessible active sites. Pore size distributions (Figure 2g) reveal predominant mesopores centered at 6.8 nm for $Al_{0.15}$-Co_xO_v and 5.3 nm for $Al_{0.45}$-Co_xO_v, both within the mesoporous range (2–50 nm). Although the pore diameter decreases slightly with increasing Al content, the open mesoporous framework still facilitates efficient diffusion and transport of electrolyte ions, synergistically enhancing the electrochemical activity. High-resolution TEM imaging (Figure 2h) reveals lattice fringes with a spacing of 0.287 nm, matching the (222) planes of Co_9S_8, while Figure 2i displays fringes separated by 2.48 nm, indexed to the (400) planes of the same phase. These observations collectively confirm the high crystallinity of the as-synthesized Co_9S_8.

Figure 3a shows the cyclic voltammetry (CV) curves of the undoped Co_xS_v electrode of sample Al_0-Co_xS_v at scan rates ranging from 5 to 50 mV s^{-1}. A very distinct feature can be observed—the peaks of the oxidation-reduction reaction. These peaks gradually increase as the scan rate rises, which clearly indicates that a specific pseudocapacitance characteristic is at play. Figure 4b,c depicts the galvanostatic charge-discharge (GCD) curves of the Co_xS_v electrode at different current densities. All the GCD curves exhibit extremely excellent symmetry, which fully demonstrates the outstanding reversibility of the said electrode. This indicates that the electrode can maintain stable performance during the electrochemical process and effectively conduct charge transfer, thus enabling efficient electrochemical oxidation or reduction reactions. By calculating the charge-discharge times of each electrode under different test conditions in Figure 3b,c, the specific capacitance can be obtained. Under the test conditions of 1, 2, 4, 6, 8, and 10 mA cm^{-2}, the areal specific capacitances of the Co_xS_v electrode are 282.7, 263.2, 225.6, 189.6, 166.4,

https://doi.org/10.1021/acs.energyfuels.5c04896
Energy Fuels 2026, 40, 3770–3780

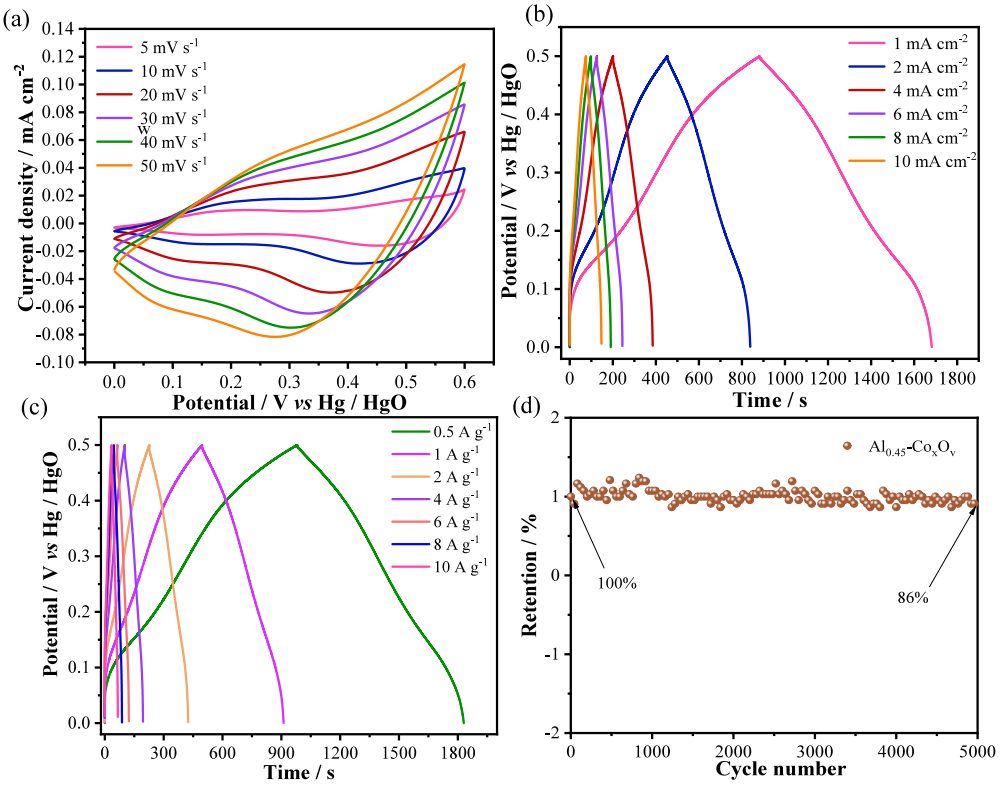

Figure 4. (a) CV curves of the electrode at different scan rates. (b, c) GCD curves of the electrode at different areal current densities and different mass current densities. (d) Chronoamperometric stability tests of $Al_{0.45}$-Co_xO_v.

and 164 C cm^{-2} respectively. Under the test conditions of 0.5, 1, 2, 4, 6, 8, and 10 A g^{-1}, the gravimetric specific capacitances of the Co_xS_v electrode can reach 317.8, 280.2, 240.8, 195.2, 160.8, 131.2, and 128 C g^{-1} respectively.

Figure 3d represents the CV curves of the Co_xS_v electrode of sample $Al_{0.15}$-Co_xS_v doped with 0.15 mmol of Al ions at scan rates from 5 to 50 mV s^{-1}. The areas of all the CV curves in the figure increase as the scan rate rises, showing typical pseudocapacitance behavior. Figure 3e,f shows the GCD curves of the Co_xS_v electrode at different current densities. All the GCD curves display good symmetry, indicating that the electrode has good reversibility and electrochemical performance. By calculating the charge-discharge times of different electrodes under different test conditions in Figure 3e,f, under the test conditions of 1, 2, 4, 6, 8, and 10 mA cm^{-2}, the areal specific capacitances of the Co_xS_v electrode are 776, 749.4, 695.2, 682.2, 640.8, and 606 C cm^{-2} respectively. Under the test conditions of 0.5, 1, 2, 4, 6, 8, and 10 A g^{-1}, the gravimetric specific capacitances of the Co_xS_v electrode can reach 771.4, 734.4, 705.6, 657.6, 637.2, 616, and 582 C g^{-1} respectively.

Figure 3g shows the CV curves of the Co_xS_v electrode of sample $Al_{0.3}$-Co_xS_v doped with 0.3 mmol of Al ions at scan rates from 5 to 50 mV s^{-1} (Table 1). The areas of all the CV curves in the figure increase as the scan rate rises, demonstrating typical pseudocapacitance behavior. Figure 3h,i presents the GCD curves of the Co_xS_v electrode at different current densities. All the GCD curves have good symmetry, with the discharge time being close to the charge time, indicating that the electrode has good reversibility and electrochemical performance. By calculating the charge-discharge times of different electrodes under different test conditions in Figure 3h,i, under the test conditions of 1, 2, 4, 6, 8, and 10 mA cm^{-2}, the areal specific capacitances of the Co_xS_v electrode are 601.6, 591.8, 580, 553.8, 536, and 520 C cm^{-2} respectively. Under the test conditions of 0.5, 1, 2, 4, 6, 8, and 10 A g^{-1}, the gravimetric specific capacitances of the Co_xS_v electrode can reach 588.4, 580, 572.4, 528.8, 496.8, 481.6, and 486 C g^{-1} respectively.

Figure 4a shows the CV curves of the Co_xS_v electrode of $Al_{0.45}$-Co_xS_v doped with 0.45 mmol of Al ions at scan rates from 5 to 50 mV s^{-1}. The areas of all the CV curves in the figure increase as the scan rate rises, showing typical pseudocapacitance behavior. Figure 4b,c shows the GCD curves of the Co_xS_v electrode at different current densities. All the GCD curves exhibit extremely excellent symmetry, which fully demonstrates the outstanding reversibility of the said electrode. This indicates that the electrode can maintain stable performance during the electrochemical process and effectively conduct charge transfer, thus enabling efficient electrochemical oxidation or reduction reactions. By calculating the charge-discharge times of each electrode under different test conditions in Figure 4b,c to obtain the specific capacitance, under the test conditions of 1, 2, 4, 6, 8, and 10 mA cm^{-2}, the areal specific capacitances of the Co_xS_v electrode are 800.6, 778.4, 752, 724.8, 768, and 712 C cm^{-2} respectively. Under the test conditions of 0.5, 1, 2, 4, 6, 8, and 10 A g^{-1}, the gravimetric specific capacitances of the Co_xS_v electrode can reach 853.8,

Table 1. Performance of the Samples

materials	area ratio capacity	mass specific capacity
Al_0-Co_xS_v	282.7 cm^{-2} (1 mA cm^{-2})	317.8 C g^{-1} (0.5 A g^{-1})
$Al_{0.15}$-Co_xS_v	776 C cm^{-2} (1 mA cm^{-2})	771.4 C g^{-1} (0.5 A g^{-1})
$Al_{0.3}$-Co_xS_v	601.6 C cm^{-2} (1 mA cm^{-2})	588.4 C g^{-1} (0.5 A g^{-1})
$Al_{0.45}$-Co_xS_v	800.6 C cm^{-2} (1 mA cm^{-2})	853.8 C g^{-1} (0.5 A g^{-1})

https://doi.org/10.1021/acs.energyfuels.5c04896
Energy Fuels 2026, 40, 3770−3780

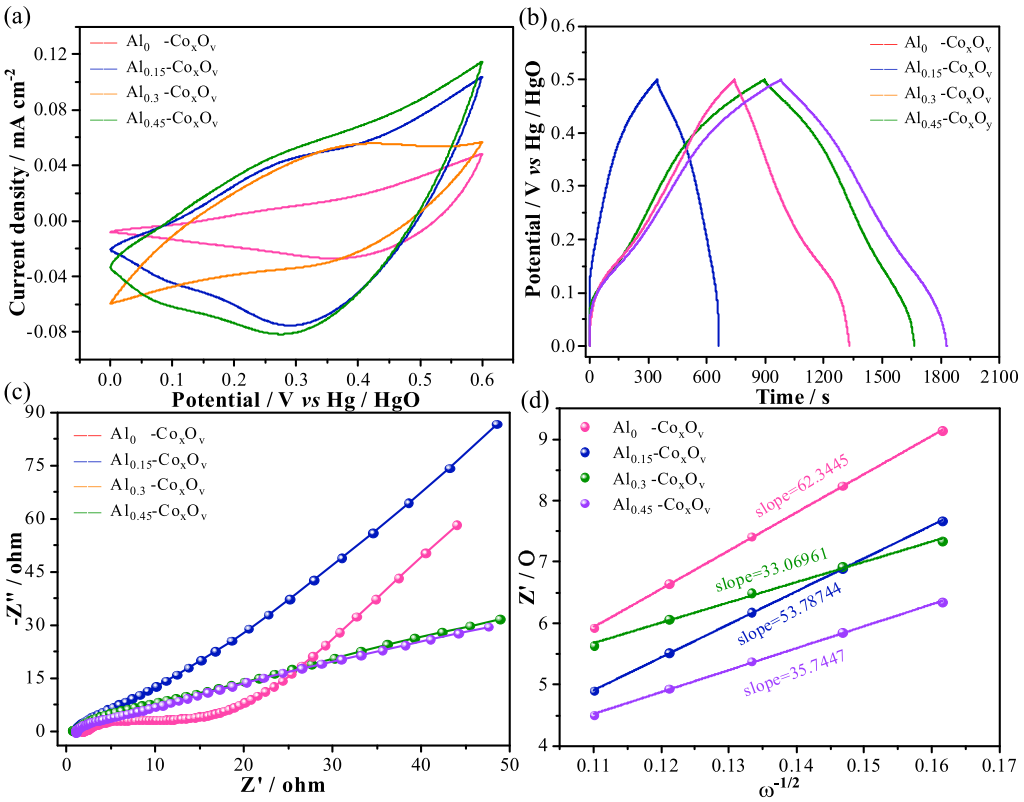

Figure 5. (a) CV curves of different electrodes at a scanning rate of 10 mV s^{-1}. (b) GCD curves of different electrodes at a current density of 1 A g^{-1}. (c) Impedance curves of different electrodes. (d) Diagram of the slope of the diagonal line in the low-frequency region of impedance.

836.4, 812.4, 777.6, 721.2, 640, and 700 C g^{-1} respectively. Figure 4d shows the capacity retention curve of the $Al_{0.45}$-Co_xS_v electrode after 5000 consecutive charge−discharge cycles, with the capacity decreasing from 100% to 86%, demonstrating its excellent cycling stability under supercapacitor operating conditions.

Figure 5a shows the cyclic voltammetry (CV) curves of different electrodes within a potential window of 0−0.6 V and at a scanning rate of 10 mV s^{-1}. It can be clearly seen that the areas of the CV curves of various material electrodes, from largest to smallest, are as follows: Co_xS_v doped with 0.45 mmol of Al ions, Co_xS_v doped with 0.15 mmol of Al ions, Co_xS_v doped with 0.3 mmol of Al ions, and Co_xS_v doped with 0 mmol of Al ions. This indicates that the specific capacitance of Co_xS_v doped with 0.45 mmol of Al ions is the largest, which fully demonstrates that the doping of Al ions has a significant impact on the specific capacitance of Co_xS_v. In particular, when doped with 0.15 and 0.45 mmol of Al ions, the increasing trend of the specific capacitance is relatively obvious. Figure 5b presents the galvanostatic charge-discharge (GCD) curves of different electrodes within a potential window of 0−0.5 V and at a current density of 1 A g^{-1} (Table 4). It can be clearly observed that the discharge time of the Co_xS_v electrode doped with 0.45 mmol of Al ions is the longest, reaching 418.2 s. Through calculation, the areal specific capacitance and gravimetric specific capacitance of the Co_xS_v electrode doped with 0.45 mmol of Al ions are greater than those of other samples. Figure 5c shows the electrochemical impedance spectroscopy (EIS) of different electrode materials in the frequency range of 0.01−100 kHz. All the EIS curves in the figure consist of a quasi-semicircle and an inclined line. The slope of the inclined line in the low-frequency region reflects the resistance of electron transfer and ion diffusion in the electrolyte solution, while the quasi-semicircle in the high-frequency region represents the charge transfer resistance between the electrode and the electrolyte solution. $Al_{0.15}$-Co_xS_v exhibits a higher slope in the low-frequency region, indicating that it has lower ion transport resistance. Figure 5d indicates that as the amount of doped Al increases, the slope of the low-frequency region in Figure 5c gradually decreases, which means that the performance of electron transfer and ion diffusion will decline. The increase in Al content significantly enhances the capacitive performance of Al−Co_xO_v materials, a phenomenon that is evidenced by the morphological transformation from nanorod arrays to nanosheet structures. This structural evolution is primarily attributed to the modulation of crystal symmetry induced by Al incorporation as well as the expansion of interlayer spacing.[24] Compared to the original structure, the nanosheet morphology offers a larger specific surface area and exposes more electrochemically active sites, thereby effectively enhancing the pseudocapacitive response. Moreover, the enlarged interlayer spacing facilitates the rapid diffusion and transport of electrolyte ions, further improving the electrochemical kinetic performance of the material.

All the electrocatalytic water splitting tests were carried out by using a standard three-electrode system to conduct electrocatalytic oxygen-evolution tests on the electrodes in a 1 M KOH solution. The Co_xS_v electrodes doped with 0, 0.15, 0.3, and 0.45 mmol of Al ions were used as the working electrodes, while the silver/silver-chloride electrode and the platinum sheet were used as the reference electrode and the counter electrode, respectively. The electrode potential was converted to the reversible hydrogen electrode (RHE) through the Nernst equation. Before performing the linear sweep

https://doi.org/10.1021/acs.energyfuels.5c04896
Energy Fuels 2026, 40, 3770−3780

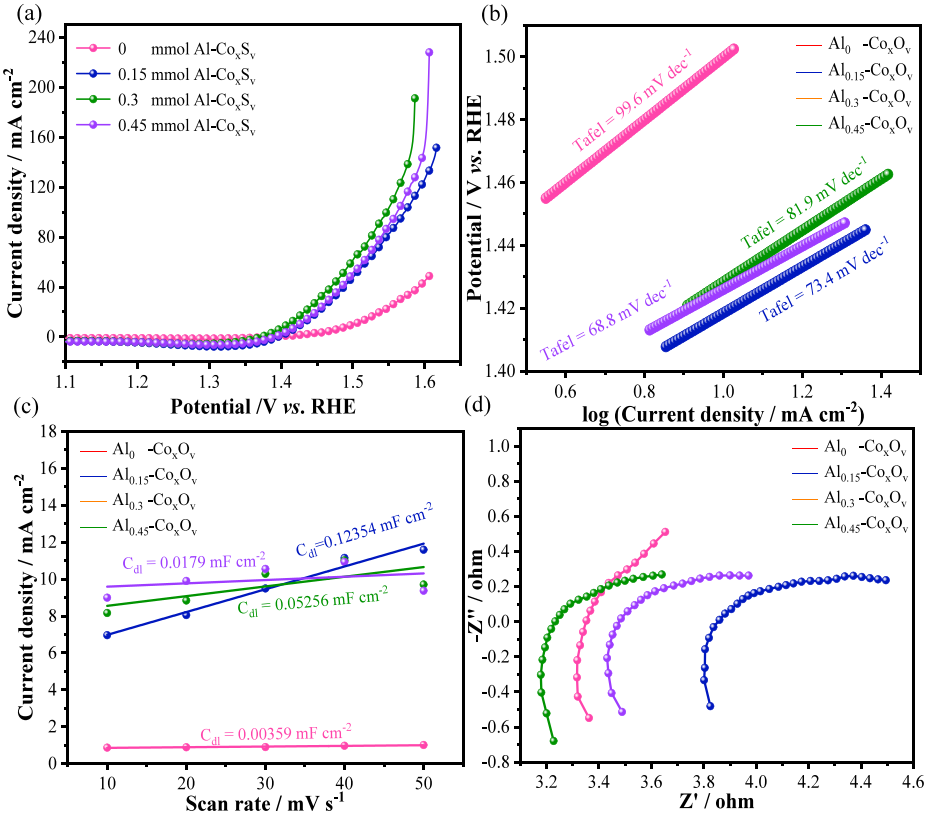

Figure 6. Electrocatalytic performances of the electrocatalysts in 1.0 M KOH. (a) LSV curves for OER. (b) Tafel plots. (c) CV curves of double-layer capacitance. (d) Nyquist plots.

voltammetry (LSV) test, as can be obtained from Figure 6a, at 10 mA cm^{-2}, the overpotentials of the Co_xS_v material electrodes with different doping amounts of 0−0.45 mmol of Al ions were 270.1 mV, 188.3 mV, 194.4 mV, and 197.7 mV, respectively. In order to explore the reaction kinetics, a Tafel plot can be drawn based on the polarization curve, so as to analyze the electrocatalytic reaction process more accurately and provide theoretical support for performance optimization. As can be seen from Figure 6b, the Tafel slopes of the four groups of samples were 99.6 mV dec^{-1}, 73.4 mV dec^{-1}, 81.9 mV dec^{-1}, and 68.8 mV dec^{-1}, respectively. The Tafel slope of Co_xS_v doped with 0.45 mmol of Al ions was lower than that of the other three groups, indicating that its reaction kinetics was more favorable.

The electrochemical active surface area (ECSA), as a key technical indicator, reflects the ability of the catalyst surface to generate electrochemical reactions during the electrochemical process and is an important basis for evaluating the efficiency and stability of the catalyst. The double-layer capacitance (Cdl) plays a core role in this parameter. The electrochemical activity of the electrode material is quantified by calculating the double-layer capacitance of the electrode material to the electrolyte ions. Simply put, the larger the Cdl, the stronger the electrocatalytic potential of the electrode material. Measuring the double-layer capacitance can effectively evaluate the electrochemical active surface area of the electrocatalyst, thus enabling a deep understanding of its reaction kinetic characteristics. As shown in Figure 6c, the Cdl (0.12354 mF cm^{-2}) of Co_xS_v doped with 0.15 mmol of Al ions was higher than that of the other three electrocatalysts. A high Cdl value indicates that this sample has a high ECSA. That is, during the catalytic reaction process, the Co_xS_v sample doped with 0.15 mmol of Al ions has a large available active specific surface area and a high density of active sites. This means that this electrode material exhibits excellent adsorption ability for water molecules. The OER process involves a four-electron transfer mechanism, which typically results in a high overpotential and significant energy loss for water splitting.[25,26]

$$* + OH^- \rightarrow {}^*OH + e^- \quad (1)$$

$${}^*OH \rightarrow {}^*O + H_2O + e^- \quad (2)$$

$${}^*O + OH^- \rightarrow {}^*OOH + e^- \quad (3)$$

$${}^*OOH \rightarrow O_2 + * + H^+ + e^- \quad (4)$$

At the initial stage of the reaction, hydroxide ions (OH^-) from water are first adsorbed onto the catalyst surface, forming an active intermediate ($*OH^-$) accompanied by the loss of one electron. Subsequently, the *OH- intermediate undergoes further oxidation, resulting in the release of a proton (H^+) and the generation of a water molecule (H_2O) along with an additional electron. This process leads to the formation of adsorbed oxygen species (*O). The adsorbed oxygen species (*O) then reacts with another hydroxide ion (OH^-) to form a new intermediate species (*OOH). Following subsequent oxidation, the OOH intermediate ultimately releases an O_2 molecule while regenerating the catalytic active sites (*), thereby sustaining the continuous operation of the catalytic cycle.

Figure 6d shows the Nyquist plots of each electrode. All the Nyquist plots are in a semi-circular shape. The semicircle of the curve represents the high-frequency region, reflecting the

https://doi.org/10.1021/acs.energyfuels.5c04896
Energy Fuels 2026, 40, 3770−3780

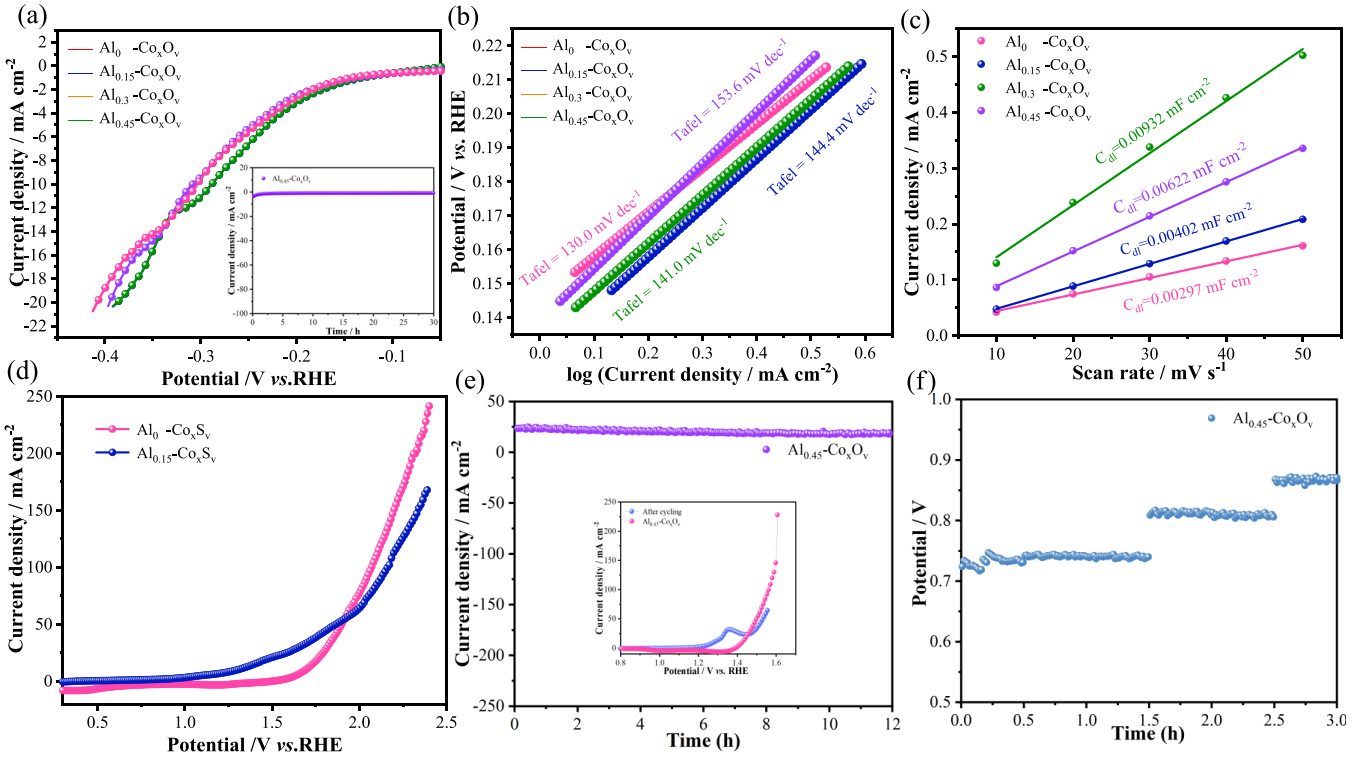

Figure 7. Electrocatalytic performances of the electrocatalysts in 1.0 M KOH. (a) LSV curves for HER. (b) Tafel plots. (c) CV curves of double-layer capacitance. (d) Overall water splitting performance of the electrocatalyst LSV curves in 1.0 M KOH. (e) Chronoamperometric stability tests of the OER. (f) Cycling under different potentials.

electrode reaction kinetics (i.e., the charge transfer process). Compared with other Co_xS_v samples, the Co_xS_v sample doped with 0.15 mmol of Al ions has a smaller semi-circular region, which proves that it has a faster charge transfer and ion-transfer rate during the electrocatalytic process, thus demonstrating excellent oxygen-evolution reaction performance.

The electrocatalytic water splitting test was also carried out by using a standard three-electrode system to conduct electrocatalytic hydrogen evolution tests on the electrodes in a 1 M KOH solution. The Co_xS_v electrodes doped with 0, 0.15, 0.3, and 0.45 mmol of Al ions were used as the working electrodes, with the silver/silver-chloride electrode and the platinum sheet serving as the reference electrode and the counter electrode, respectively.

As can be obtained from Figure 7a, at 10 mA cm^{-2}, the overpotentials of the Co_xS_v material electrodes with different doping amounts of 0−0.45 mmol of Al ions were 303 mV, 228.3 mV, 293.3 mV, and 309.3 mV, respectively. The lower overpotential at the same current density proves that the Co_xS_v doped with 0.15 mmol of Al ions is a HER catalyst with relatively high activity among them. In order to explore the reaction kinetics, a Tafel plot can be drawn based on the polarization curve to analyze the electrocatalytic reaction process more accurately and provide theoretical support for performance optimization. Long-term HER stability was assessed under galvanostatic conditions (Figure 7a). The electrode maintained a current density of 0.8 mA cm^{-2} for 30 h without noticeable decay, demonstrating robust electrochemical durability.

As can be seen from Figure 7b, the Tafel slopes of the four groups of samples were 130.0 mV dec^{-1}, 144.4 mV dec^{-1}, 141.0 mV dec^{-1}, and 153.6 mV dec^{-1}, respectively. The Tafel slope of Co_xS_v doped with 0 mmol of Al ions was lower than that of the other three groups, indicating that its reaction kinetics was more favorable. As shown in Figure 7c, the Cdl (0.00932 mF cm^{-2}) of Co_xS_v doped with 0.3 mmol of Al ions was higher than that of the other three electrocatalysts. A high Cdl value indicates that this sample has a high ECSA. Moreover, the Cdl (0.00932 mF cm^{-2}) of Co_xS_v doped with 0.3 mmol of Al ions and the Cdl (0.00622 mF cm^{-2}) of Co_xS_v doped with 0.45 mmol of Al ions were larger than the Cdl (0.00402 mF cm^{-2}) of Co_xS_v doped with 0.15 mmol of Al ions, whose overpotential was the smallest. This phenomenon can be attributed to the higher intrinsic activity exhibited by both materials.

Finally, we explored the performance of the prepared 0.15 mmol Al-ion-doped Co_xS_v nanomaterial and the undoped Co_xS_v nanomaterial as water splitting electrodes, respectively. Under the condition of a 1 M KOH electrolyte, the performance of each system was tested at a scanning rate of 5 mV s^{-1}. As shown in Figure 7d, the 0.15 mmol Al-ion-doped Co_xS_v nanomaterial only requires a voltage of 1.30 V to achieve water splitting, compared with 1.69 V for the undoped Co_xS_v nanomaterial. This fully demonstrates that the doping treatment significantly improves the performance of the Co_xS_v nanomaterial in overall water splitting. As shown in Figure 7e, the $A_{l0.45}$-Co_xS_v catalyst exhibits excellent OER stability, with a voltage drop of only 0.04 V after 30 h of continuous operation at constant current. At a current density of 50 mA cm^{-2}, further confirming its exceptional durability. The chronoamperometric test conducted at 0.74, 0.815, and 0.87 V (vs RHE) demonstrates negligible current fluctuations over 3 h of continuous operation, highlighting the exceptional electrochemical stability of the material.

https://doi.org/10.1021/acs.energyfuels.5c04896
Energy Fuels 2026, 40, 3770−3780

4. CONCLUSIONS

In this thesis, $ZnCo_2O_4$ and its composite materials, as well as Co_xS_v nanomaterials, were taken as the research objects. Samples with different ratios were prepared respectively, and a series of electrochemical performance characterizations were carried out on them. The influences of different experimental conditions on the structure and electrochemical properties of the prepared electrode materials were explored. Through the electrocatalytic water splitting oxygen-evolution tests on the Co_xS_v electrodes doped with different concentrations of Al ions (Tables 2 and 3), it was obtained that the Cdl (0.12354 F cm^{-2}) of the Co_xS_v doped with 0.15 mmol of Al ions was higher than that of the other three groups of experiments. A high Cdl value indicates that this sample has a high ECSA. That is, during the catalytic reaction process, the Co_xS_v sample doped with 0.15 mmol of Al ions has a large available active specific surface area and a high density of active sites. This means that this electrode material exhibits excellent adsorption ability for water molecules.

Table 2. Electrocatalytic Performance of the Samples

materials	overpotential	electrolyte	ref.
NiCoP/NF	280 (10 mA cm^{-2})	1.0 M KOH	27
FeCoO-NF	244 (10 mA cm^{-2})	1.0 M KOH	28
$NiCo_2O_4$	290 (10 mA cm^{-2})	1.0 M NaOH	29
CoS_2HNSs	290 (10 mA cm^{-2})	1.0 M KOH	30
Co−150S/NF	105 (−10 mA cm^{-2})	1.0 M KOH	41
CoS_2@Mo-VS_4@CC	73 (−10 mA cm^{-2})	0.5MH_2SO_4	44
Al−Co_xO_v	188.3(10 mA cm^{-2})	1.0 M KOH	**this work**
Al−Co_xO_v	228.3(−10 mA cm^{-2})	1.0 M KOH	**this work**

Table 3. Performance of the Samples

materials	overpotential-OER	overpotential-HER
Al_0-Co_xS_v	270.1 mV (10 mA cm^{-2})	303 mV (10 mA cm^{-2})
$Al_{0.15}$-Co_xS_v	188.3 mV (10 mA cm^{-2})	228.3 mV (10 mA cm^{-2})
$Al_{0.3}$-Co_xS_v	194.4 mV (10 mA cm^{-2})	293.3 mV (10 mA cm^{-2})
$Al_{0.45}$-Co_xS_v	197.7 mV (10 mA cm^{-2})	309.3 mV (10 mA cm^{-2})

Table 4. Parameters Obtained from the BET Examination

materials	BET surface area (m^2/g)	pore size (nm)
$Al_{0.15}$-Co_xS_v	20.6423	6.79
$Al_{0.45}$-Co_xS_v	34.2792	5.31

AUTHOR INFORMATION

Corresponding Authors

Kai Jia − *Liaoning University of Technology, Jinzhou 121001, P. R. China*; Email: kai311@lnut.edu.cn

Rong-Da Zhao − *Liaoning University of Technology, Jinzhou 121001, P. R. China*; orcid.org/0000-0002-1637-0909; Email: Rongdazhaoln@126.com

Depeng Zhao − *Liaoning University of Technology, Jinzhou 121001, P. R. China; School of New Energy, Shenyang Institute of Engineering, Shenyang 110136, P. R. China*; orcid.org/0000-0001-8054-3926; Email: hellodepeng@163.com

Lihua Miao − *School of Medical Information Engineering, Shenyang Medical College, Shenyang, Liaoning 110034, P. R. China*; orcid.org/0000-0001-8244-5211; Email: miaolihua@163.com

Authors

Heran Ren − *Liaoning University of Technology, Jinzhou 121001, P. R. China*

Zihan Lv − *Liaoning University of Technology, Jinzhou 121001, P. R. China*

Zhiqiang Yin − *School of New Energy, Shenyang Institute of Engineering, Shenyang 110136, P. R. China*

Songlin Xu − *Liaoning University of Technology, Jinzhou 121001, P. R. China*

Huiya Zhou − *Liaoning University of Technology, Jinzhou 121001, P. R. China*

Complete contact information is available at: https://pubs.acs.org/10.1021/acs.energyfuels.5c04896

Notes

The authors declare no competing financial interest.

ACKNOWLEDGMENTS

This work was supported by the Project of Education Department of Liaoning Province (No. LJKMZ20220959), the National Natural Science Foundation of China (No. 51971106). Science and Technology Innovation Talent Project of Liaoning Provincial Department of Education (LJ222411632049, LJ222411632081).

REFERENCES

(1) Yang, J.; Yu, C.; Fan, X.; Liang, S.; Li, S.; Huang, H.; Ling, Z.; Hao, C.; Qiu, J. Electroactive edge site-enriched nickel−cobalt sulfide into graphene frameworks for high-performance asymmetric supercapacitors. *Energy Environ. Sci.* **2016**, *9*, 1299−1307.

(2) Martínez-Periñán, E.; Down, M. P.; Gibaja, C.; Lorenzo, E.; Zamora, F.; Banks, C. E. Antimonene: A Novel 2D Nanomaterial for Supercapacitor Applications. *Adv. Energy Mater.* **2018**, *8*, 1702606.

(3) Xu, G.; Zhang, Z.; Qi, X.; Ren, X.; Liu, S.; Chen, Q.; Huang, Z.; Zhong, J. Hydrothermally synthesized $FeCo_2O_4$ nanostructures: Structural manipulation for high-performance all solid-state supercapacitors. *Ceram. Int.* **2018**, *44*, 120−127.

(4) Chen, H.; Jiang, J.; Zhang, L.; Wan, H.; Qi, T.; Xia, D. Highly conductive $NiCo_2S_4$ urchin-like nanostructures for high-rate pseudocapacitors. *Nanoscale* **2013**, *5*, 8879−8883.

(5) Chen, Z.; Augustyn, V.; Jia, X.; Xiao, Q.; Dunn, B.; Lu, Y. High-performance sodium-ion pseudocapacitors based on hierarchically porous nanowire composites. *ACS Nano* **2012**, *6*, 4319−4327.

(6) Huang, Z.; Zhang, Z.; Qi, X.; Ren, X.; Xu, G.; Wan, P.; Sun, X.; Zhang, H. Wall-like hierarchical metal oxide nanosheet arrays grown on carbon cloth for excellent supercapacitor electrodes. *Nanoscale* **2016**, *8*, 13273−13279.

(7) Zhao, J.; Gong, J.; Wang, G.; Zhu, K.; Ye, K.; Yan, J.; Cao, D. A self-healing hydrogel electrolyte for flexible solid-state supercapacitors. *Chem. Eng. J.* **2020**, *401*, No. 125456.

(8) Libich, J.; Máca, J.; Vondrák, J.; Čech, O.; Sedlaříková, M. Supercapacitors: Properties and applications. *J. Energy Storage* **2018**, *17*, 224−227.

(9) Liu, H.; Zhao, D.; Dai, M.; Zhu, X.; Qu, F.; Umar, A.; Wu, X. PEDOT decorated $CoNi_2S_4$ nanosheets electrode as bifunctional electrocatalyst for enhanced electrocatalysis. *Chem. Eng. J.* **2022**, *428*, No. 131183.

(10) Zhu, Y.; Lin, Q.; Zhong, Y.; Tahini, H. A.; Shao, Z.; Wang, H. Metal oxide-based materials as an emerging family of hydrogen evolution electrocatalysts. *Energy Environ. Sci.* **2020**, *13*, 3361−3392.

(11) Tian, X.; Zhao, P.; Sheng, W. Hydrogen evolution and oxidation: Mechanistic studies and material advances. *Adv. Mater.* **2019**, *31*, 1808066.

(12) Li, P.; Duan, X.; Kuang, Y.; Li, Y.; Zhang, G.; Liu, W.; Sun, X. Tuning electronic structure of NiFe layered double hydroxides with

vanadium doping toward high efficient electrocatalytic water oxidation. *Adv. Energy Mater.* **2018**, *8*, 1703341.
(13) Prabu, M.; Ketpang, K.; Shanmugam, S. Hierarchical nanostructured $NiCo_2O_4$ as an efficient bifunctional non-precious metal catalyst for rechargeable zinc-air batteries. *Nanoscale* **2014**, *6*, 3173−3181.
(14) Wang, Y.; Ding, W.; Chen, S.; Nie, Y.; Xiong, K.; Wei, Z. Cobalt carbonate hydroxide/C: an efficient dual electrocatalyst for oxygen reduction/evolution reactions. *Chem. Commun.* **2014**, *50*, 15529−15532.
(15) Zhang, L.; Li, Y.; Peng, J.; Peng, K. Bifunctional $NiCo_2O_4$ porous nanotubes electrocatalyst for overall water-splitting. *Electrochim. Acta* **2019**, *318*, 762−769.
(16) Meher, S. K.; Rao, G. R. Ultralayered Co_3O_4 for high-performance supercapacitor applications. *J. Phys. Chem. C* **2011**, *115*, 15646−15654.
(17) Zhang, G.; Lou, X. W. General Solution Growth of Mesoporous $NiCo_2O_4$ Nanosheets on Various Conductive Substrates as High-Performance Electrodes for Supercapacitors. *Adv. Mater.* **2013**, *25*, 976−979.
(18) Yan, J.; Fan, Z.; Sun, W.; Ning, G.; Wei, T.; Zhang, Q.; Zhang, R.; Zhi, L.; Wei, F. Advanced Asymmetric Supercapacitors Based on $Ni(OH)_2$/Graphene and Porous Graphene Electrodes with High Energy Density. *Adv. Funct. Mater.* **2012**, *22*, 2632−2641.
(19) Dai, C. S.; Chien, P. Y.; Lin, J. Y.; Chou, S. W.; Wu, W. K.; Li, P. H.; Wu, K. Y.; Lin, T. W. Hierarchically structured Ni3S2/carbon nanotube composites as high performance cathode materials for asymmetric supercapacitors. *ACS Appl. Mater. Interfaces* **2013**, *5*, 12168−12174.
(20) Ryu, K. S.; Kim, K. M.; Park, N. G.; Park, Y. J.; Chang, S. H. Symmetric redox supercapacitor with conducting polyaniline electrodes. *J. Power Sources* **2002**, *103*, 305−309.
(21) Zhou, X.; Li, J.; Zhou, G.; Huang, W.; Zhang, Y.; Yang, J.; Pang, H.; Zhang, M.; Sun, D.; Tang, Y.; Xu, L. Manipulating d-d orbital hybridization induced by Mo-doped Co9S8 nanorod arrays for high-efficiency water electrolysis. *J. Energy Chem.* **2024**, *93*, 592−600.
(22) More, S.; Joshi, B.; Khadka, A.; et al. Oriented attachment of carbon/cobalt−cobalt oxide nanotubes on manganese-doped carbon nanofibers for flexible symmetric supercapacitors. *Appl. Surf. Sci.* **2023**, *615*, No. 156386.
(23) Khadka, A.; Samuel, E.; Joshi, B.; Kim, Y. I.; Aldalbahi, A.; El-Newehy, M.; Lee, H. S.; Yoon, S. S.; Chhetri, K.; et al. Bimetallic CoMoO4 nanosheets on freestanding nanofiber as wearable supercapacitors with long-term stability. *Int. J. Energy Res.* **2023**, 1.
(24) Xu, Z.; Li, X.; Sun, S.; Wang, X.; Zhang, Z.; Li, H.; Yin, S. High mass loading NiCoAl layered double hydroxides with interlayer spacing and interface regulation for high-capacity and long-life supercapacitors. *J. Power Sources* **2022**, *546*, No. 231982.
(25) Shaikh, J. S.; Rittiruam, M.; Saelee, T.; Márquez, V.; Shaikh, N. S.; Khajondetchairit, P.; Pathan, S.; Kanjanaboos, P.; Taniike, T.; Nazeeruddin, M. K.; Praserthdam, P.; Praserthdam, S. First-principles and experimental insight of high-entropy materials as electrocatalysts for energy-related applications: Hydrogen evolution, oxygen evolution, and oxygen reduction reactions. *Mater. Sci. Eng. R Rep.* **2024**, *160*, No. 100813.
(26) Pathan, S. C.; Shaikh, J. S.; Shaikh, N. S.; Márquez, V.; Rittiruam, M.; Saelee, T.; Khajondetchairit, P.; Mali, S. S.; Patil, J. V.; Hong, C. K.; Praserthdam, P.; Praserthdam, S. Electrocatalytic overall water splitting based on (ZnNiCoFeY)xOy high-entropy oxide supported on MoS2. *South Afr. J. Chem. Eng.* **2024**, *48*, 425−435.
(27) Liang, H.; Gandi, A. N.; Anjum, D. H.; Wang, X.; Schwingenschlögl, U.; Alshareef, H. N. Plasma-Assisted Synthesis of NiCoP for Efficient Overall Water Splitting. *Nano Lett.* **2016**, *16* (12), 7718−7725.
(28) Bandal, H. A.; Jadhav, A. R.; Tamboli, A. H.; Kim, H. Bimetallic iron cobalt oxide self-supported on Ni-Foam: An efficient bifunctional electrocatalyst for oxygen and hydrogen evolution reaction. *Electrochim. Acta* **2017**, *249*, 253−262.
(29) Gao, X.; Zhang, H.; Li, Q.; Yu, X.; Hong, Z.; Zhang, X.; Liang, C.; Lin, Z. Hierarchical NiCo2O4 Hollow Microcuboids as Bifunctional Electrocatalysts for Overall Water-Splitting. *Angew. Chem., Int. Ed.* **2016**, *55* (21), 6290−6294.
(30) Ma, X.; Zhang, W.; Deng, Y.; Zhong, C.; Hu, W.; Han, X. Phase and composition controlled synthesis of cobalt sulfide hollow nanospheres for electrocatalytic water splitting. *Nanoscale* **2018**, *10* (10), 4816−4824.
(31) Zhang, R.; Tang, C.; Kong, R.; Du, G.; Asiri, A. M.; Chen, L.; Sun, X.; et al. Al Doped CoP nanoarray: a durable water-splitting electrocatalyst with superhigh activity. *Nanoscale* **2017**, *9*, 4793.
(32) Xu, J.; Sousa, J. P. S.; Mordvinova, N. E.; Costa, J. D.; Petrovykh, D. Y.; Kovnir, K.; Lebedev, O. I.; Kolen'ko, Y. V.; et al. Al-induced in situ formation of highly active nanostructured water-oxidation electrocatalyst based on Ni phosphide. *ACS Catal.* **2018**, *8*, 2595.
(33) Wang, Y.; Wu, J.; Tang, Y.; Lü, X.; Yang, C.; Qin, M.; Huang, F.; Li, X.; Zhang, X. Phase-controlled synthesis of cobalt sulfides for lithium ion batteries. *ACS Appl. Mater. Interfaces* **2012**, *4* (8), 4246−4250.
(34) Ansari, S.A.; Alam, M.W.; BaQais, A.; Yewale, M. A. Exploring the effective electrochemical diclofenac sensing, energy storage, and photocatalytic capabilities of strontium-doped molybdenum oxide nanoparticles. *J. Ind. Eng. Chem.* **2025**.
(35) Ansari, S. A. Fabrication and evaluation of binder-free metal-molybdate electrodes for improved energy storage and hydrogen evolution applications. *J. Power Sources* **2025**, *646*, No. 237185.
(36) Ansari, S. A.; Parveen, N.; Ansari, M. Z.; Alsulaim, G. M.; Alam, M. W.; Khan, M. Y.; Umar, A.; Hussain, I.; Zhang, K. Exploring recent advances in the versatility and efficiency of carbon materials for next generation supercapacitor applications: A comprehensive review. *Prog. Mater. Sci.* **2025**, *154*, No. 101493.
(37) Al-Abawi, B. T.; Parveen, N.; Ansari, S. A.; Al-Dosari, H. A.; Alshaikh, H. K.; Umar, A.; Ibrahim, A. A.; Akbar, S.; Katkar, P. K. Emerging Trends in Nickel Sulfide Electrodes for High-Performance Supercapacitors: Synthesis, Mechanisms, and Nanocomposite Innovations. *Int. J. Energy Res.* **2025**, 5331742.
(38) Parveen, N. Enhanced energy storage using bio-waste derived carbon and three-dimensional $NiCo_2O_4$ structures in asymmetric supercapacitors. *J. Ind. Eng. Chem.* **2025**, *150*, 824−836.
(39) Parveen, N.; Ansari, S. A.; Alnahdi, K. M.; Hammud, H. H.; Aljamhi, W. A.; Alam, M. W.; Adil, S. F.; Al Zoubi, W. Eco-friendly synthesis and applications of graphene-titanium dioxide nanocomposites for pollutant degradation and energy storage. *J. Photochem. Photobiol. A: Chem.* **2025**, *459*, No. 116096.
(40) Parveen, N.; Da'na, E.; Taha, A. Sustainable fabrication of Fe_2O_3/C nanoparticles via Acacia nilotica extract for enhanced supercapacitor performance. *Nanotechnology* **2025**, *36*, 115704.
(41) Mise, Y.; Wang, S.; Shi, W.; et al. Synergistic sulfur engineering in Amorphous Co−S nanoparticles via ChCl−EG DES−mediated synthesis for efficient overall water splitting. *Ionics* **2025**, *31*, 8221−8233.
(42) Chi, L. P.; Niu, Z. Z.; Zhang, X. L.; et al. Stabilizing indium sulfide for CO_2 electroreduction to formate at high rate by zinc incorporation. *Nat. Commun.* **2021**, *12*, 5835.
(43) Huang, Z. F.; Song, J.; Li, K.; Tahir, M.; Wang, Y. T.; Pan, L.; Wang, L.; Zhang, X.; Zou, J. J. Hollow Cobalt-Based Bimetallic Sulfide Polyhedra for Efficient All-pH-Value Electrochemical and Photocatalytic Hydrogen Evolution. *J. Am. Chem. Soc.* **2016**, *138* (4), 1359−1365.
(44) Zhao, X.; Wang, J.; Zhang, Y.; Dong, Y.; Yin, Y.; Yu, Z.; Ge, G.; Yu, J.; Mu, S. CoS_2 Hybridized Mo-Doped VS_4 Core−Shell Three-Dimensional Nanoarrays for Efficient Hydrogen Evolution Reaction. *J. Alloys Compd.* **2025**, *1020*, No. 179346.

https://doi.org/10.1021/acs.energyfuels.5c04896
Energy Fuels 2026, 40, 3770−3780